Article

High-Performance Layered Oxides for Sodium-Ion Batteries Achieved through Combined Aluminum Substitution and Surface Treatment

Mariya Kalapsazova [1,*], Rositsa Kukeva [1], Sonya Harizanova [1], Pavel Markov [1], Diana Nihtianova [1,2], Ekaterina Zhecheva [1] and Radostina Stoyanova [1,*]

[1] Institute of General and Inorganic Chemistry, Bulgarian Academy of Sciences, 1113 Sofia, Bulgaria
[2] Institute of Mineralogy and Crystallography, Bulgarian Academy of Sciences, 1113 Sofia, Bulgaria
* Correspondence: maria_l_k@svr.igic.bas.bg (M.K.); radstoy@svr.igic.bas.bg (R.S.); Tel.: +359-2-9793915 (R.S.)

Abstract: Layered sodium transition metal oxides belong to electrode materials for sodium-ion batteries that combine, in a better way, high performance with environmental requirements. However, their cycling stability is still far from desirable. Herein, we demonstrate a rational approach to control the cycling stability of sodium-deficient nickel manganese oxides, $Na_{2/3}Ni_{1/2}Mn_{1/2}O_2$, with two- and three-layer stacking through Al substitution and Al_2O_3 treatment. Layered $Na_{2/3}Ni_{1/2}Mn_{1/2}O_2$ oxide displays a limited ability to accommodate aluminum in its structure (i.e., up to 8 at. %). The substitution of Ni ions with electrochemically inactive Al^{3+} ions and keeping the amount of Mn ions in $Na_{2/3}Ni_{1/2-x}Al_xMn_{1/2}O_2$ leads to the stabilization of the two-layer stacking and favors the participation of lattice oxygen in the electrochemical reaction in addition to Ni ions. This results in an increase in the specific capacity of the Al-substituted oxides. Furthermore, the kinetics of the cationic migration between layers occurring during oxide cycling was manipulated by oxide morphology. The best cycling stability is observed for $Na_{2/3}Ni_{0.42}Al_{0.08}Mn_{1/2}O_2$ having a column-like morphology of stacked plate-like particles along the common faces. The treatment of the layered oxides with Al_2O_3 mitigates the Mn dissolution reaction during electrode cycling in the $NaPF_6$-based electrolyte, thus contributing to a high cycling stability.

Keywords: layered oxide; XRD analysis; SEM analysis; EPR spectroscopy; aluminum substitution; Al_2O_3 surface treatment; redox reactions; sodium-ion batteries; cycling stability

1. Introduction

To transform sodium-ion batteries into the technology of choice for grid-scale energy storage, there is a need to identify electrode materials that unify high performance with a low environmental footprint and high safety [1,2]. Sodium-deficient transition metal oxides (Na_xTMO_2) are the most perspective-positive electrodes since they display the unique property of delivering large capacities at high potentials, as well as containing non-critical raw elements [3,4]. This is a consequence of their propensity to adopt flexible layered structures where Na^+ ions migrate easily and quickly between the layers composed of Mn, Ni and Fe ions with different oxidation states [5]. However, their cycling stability is still far from desirable [3–5]. To improve cycling stability, several structural approaches have been proposed [6,7]. One of them concerns the substitution of transition metal ions with light metal ions [8]. The improvement of the performance of Na_xTMO_2 is a result of the stabilization of the layered structure upon Na^+ extraction and insertion [9], the control of the cationic order inside the transition metal layers [10,11], the reduction of the Jahn–Teller distortion of Mn^{3+} [12], the activation of the oxygen redox activity in addition to that of transition metal ions [13], and the enhancement of Na^+ diffusion [14]. Among light metal ions, the most widely studied are Mg^{2+}, Zn^{2+} and Al^{3+}, all of which are electrochemically

inactive [15–20]. The aluminum exhibits a specific effect in improving Na^+ diffusion kinetics in layered oxides by enlarging the space between TM layers [21,22].

The second approach is based on the surface modification of layered oxides by electrochemically inactive oxides such as Al_2O_3, MgO, ZnO, CeO_2, phosphates, etc. [23]. Aluminum oxide is of primary technological interest due to its simple synthesis, relatively high Na^+ ion diffusivity in $Na_xAl_2O_3$ and low cost [24]. The main idea of using an A_2O_3 coating is to prevent the oxide surface from interacting with the electrolyte, especially at high potentials; to modify the degradation pathways of the cathode surface from hydrogen fluoride (HF) attack; and to tune the structural stresses occurring during Na^+ extraction/insertion cycling [25–27]. In addition, oxygen-storage modifiers such as CeO_2 play a new role, which consists of the stabilization of oxygen redox activity through the oxide buffer supplying and receiving oxygen during alkali ion intercalation [28]. The phosphate coating (such as $AlPO_4$) of layered oxides serves to stabilize the surface by avoiding element dissolution, as well as by suppressing the dissolution–migration–deposition process in full sodium-ion cells [29]. In general, the improvement of the performance of Na_xTMO_2 can be achieved through the rational control of metal substitution and surface modifications.

This study aims to delve into the interplay between the structure and surface modifications and their influence on the Na storage capacity of layered sodium nickel manganese oxides, $Na_{2/3}Ni_{1/2}Mn_{1/2}O_2$. Aluminum is used as both the structure and surface modifier. The structural modification of $Na_{2/3}Ni_{1/2}Mn_{1/2}O_2$ is achieved through the selective substitution of Ni with aluminum and keeping Mn ions as Mn^{4+}. This approach is different from previously studied Al-substituted oxides, where Mn and Fe ions are targets for Al substitution [19,20,30,31]. Therefore, the first part of our study is focused on the evaluation of the concentration limits of Al substitution into $Na_{2/3}Ni_{1/2}Mn_{1/2}O_2$, and based on these results, the oxides with the highest Al content are studied electrochemically further on. The deposition of Al_2O_3 on layered oxides serves as a surface modification. Layered oxides with different layer stacking are selected for Al_2O_3 treatment: pristine $Na_{2/3}Ni_{1/2}Mn_{1/2}O_2$ and Al-substituted oxide, $Na_{0.67}Ni_{0.42}Al_{0.08}Mn_{0.50}O_2$, with a three- and two-layer sequence (i.e., *P3* and *P2* structure according to the notation of Delmas [32]). The comparison of the electrochemical properties of Al-substituted and Al_2O_3-treated oxides allows determining new correlations for the improvement of the performance of electrode materials. The changes in layered oxides upon cycling are monitored by electron paramagnetic resonance spectroscopy (EPR).

2. Materials and Methods

2.1. Materials

The Al-substituted oxides were prepared by the freeze-drying of aqueous solutions containing acetate salts of Na^+, Ni^{2+}, Mn^{2+} and Al^{3+} ions. The amount of Al varied between 4 and 16 at. %. The acetate precursors were decomposed at 400 °C to eliminate the organic part. The solid residues were ground, pelleted and annealed at 700, 800 and 900 °C for 24 h. The acetate precursors were preferred over the nitrate ones since they yield smaller particles and a narrower particle size distribution, as recently found [33].

The Al_2O_3 treatment of layered oxides was carried out by the impregnation of $P3$-$Na_{2/3}Ni_{1/2}Mn_{1/2}O_2$ and $P2$-$Na_{0.67}Ni_{0.42}Al_{0.08}Mn_{0.50}O_2$ with an aqueous solution of aluminum acetate. The Al_2O_3 content was 5 wt. %. The impregnated $P3$-$Na_{2/3}Ni_{1/2}Mn_{1/2}O_2$ and $P2$-$Na_{0.67}Ni_{0.42}Al_{0.08}Mn_{0.50}O_2$ were annealed for 2 h at 700 and 800 °C, respectively.

2.2. Methods

The structural analysis was carried out by using a powder X-ray diffractometer (Bruker Advance D8) working with CuKα radiation. The oxide morphology and chemical composition were monitored by using a scanning electron microscope (SEM, JEOL JSM 6390) equipped with the Oxford INCA energy-dispersive X-ray spectrometer. The local structure of oxides was determined by electron diffraction using the JEOL 2100 TEM microscope. The images were calculated by using Digital Micrograph software. The oxidation states

of transition metal ions were quantified by using an EPR spectrometer (Bruker EMX^{plus}) between 100 and 400 K. The electrical resistivity was measured in the framework of the van der Pauw method between 300 and 500 K using MMR's Variable Temperature Hall System (K2500-5SLP-SP).

The electrochemical experiments were performed on two- and three-electrode Swagelok-type cells. The electrodes consisted of the active material (80 wt. %), conductive additives (carbon black, Super C65, 10 wt. %) and polymer binder (polyvinylidene fluoride (PVDF), 10 wt. %). The electrode mixture was cast on an Al collector, which after drying at 80 °C overnight, was cut into electrodes with a diameter of 10 mm each. The active material was around 3.50 ± 0.5 mg/cm^2 for each electrode. The electrolyte contained 1M NaPF$_6$ in the PC. The amount of the used electrolyte was about 140 μL. A Whatman GF/D glass microfiber layer was used as a separator. All electrochemical experimenters were carried out on the Biologic VMP-3e battery cycler. To ensure reproducibility, electrochemical measurements were repeated at least twice. For ex situ EPR experiments, the subjects of the study were electrodes after 100 cycles between 1.5 and 4.8 V and, finally, discharged up to 1.5 V. The electrodes recovered from the switched-off cells were filled into EPR quartz tubes inside the glovebox (MBraun, MB-Unilab Pro SP 1500/780).

3. Results and Discussion

3.1. Al Substitution of Ni in Layered $Na_{2/3}[Ni_{1/2}Mn_{1/2}]O_2$: Concentration Limits

To understand the ability of the layered structure to uptake Al, Figure 1a gives the XRD patterns of oxides with Al content varying between 0.04 and 0.16 at. %. The index-ation of the XRD patterns reveals the formation of a phase mixture between *P2* and *P3* modifications for the Al-containing oxides. This is not observed for the unsubstituted oxide *P3*-Na$_{2/3}$Ni$_{1/2}$Mn$_{1/2}$O$_2$, where only *P3* modification is stabilized. By increasing the Al content above 8 at. % (i.e., per structural formula), an impurity phase indexed as NaAlO$_2$ appears in addition to both the *P2* and *P3* phases. This indicates a limited insertion of Al^{3+} into the layered oxide Na$_{2/3}$Ni$_{1/2}$Mn$_{1/2}$O$_2$, the upper concentration limit being 8 at. %. It is worth mentioning that the concentration limit is wider when Al^{3+} is substituted for Mn in the layered Mn-rich oxides, i.e., 40 and 22 at. % for O'3-NaMn$_{0.6}$Al$_{0.4}$O$_2$ and *P2*-Na$_{2/3}$Mn$_{7/9}$Al$_{2/9}$O$_2$ [12,34]. The oxide having the maximal Al content (i.e., 8 at. %) is studied further on.
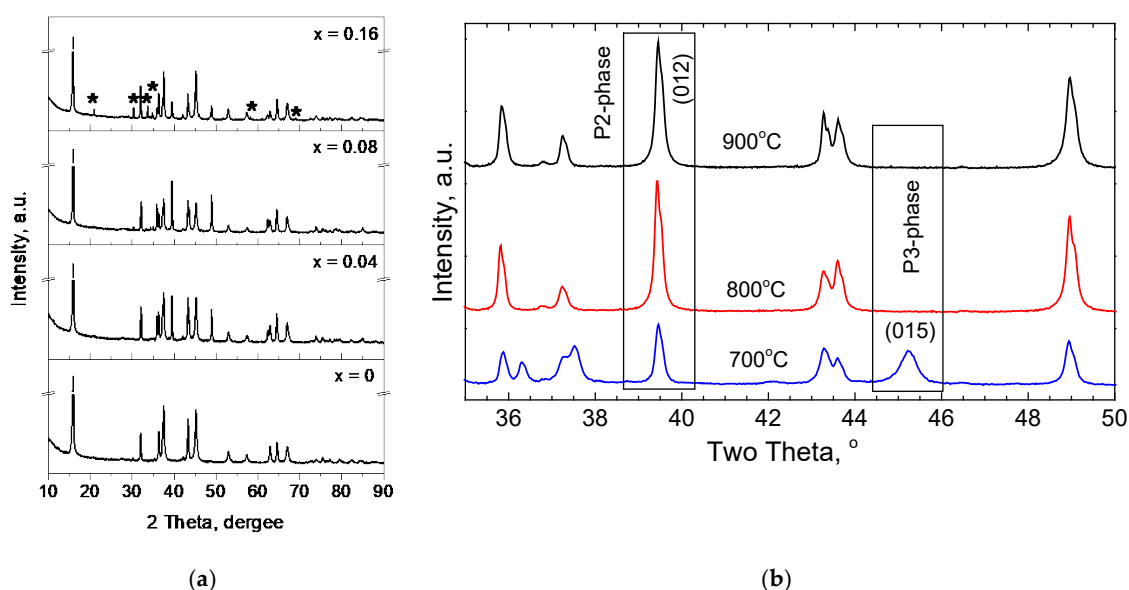

(a)   (b)

Figure 1. (a) XRD patterns of Na$_{2/3}$Ni$_{1/2-x}$Al$_x$Mn$_{1/2}$O$_2$ annealed at 700 °C. The asterisks correspond to the impurity NaAlO$_2$ phase. (b) XRD patterns of oxides containing 8 at. % of Al and annealed at 700, 800 and 900 °C. The peak indexation for *P2* and *P3* phases are shown.

The phase composition depends additionally on the annealing temperature. Figure 1b shows the XRD patterns of the oxides containing 8 at. % Al annealed at 700, 800 and 900 °C. The *P2* and *P3* phases can be clearly distinguished through the diffraction peak (012) and (015), respectively (Figure 1b). Although the oxide annealed at 700 °C contains both the *P3* and *P2* phases, the oxides annealed at 800 and 900 °C display an occurrence of *P2* modification only. In comparison with the Al-containing oxides, the *P2* modification of the unsubstituted oxides is formed at 900 °C only [35]. The XRD data disclose that Al^{3+} ions destabilize the *P3* modification at the expense of the *P2* modification.

To analyze the Al distribution in the layered structure, the lattice parameters of both the *P2* and *P3* phases are listed in Table 1. The same table also gives the lattice parameters for *P3*-$Na_{2/3}Ni_{1/2}Mn_{1/2}O_2$ and *P2*-$Na_{2/3}N_{1/3}Mn_{2/3}O_2$ used as standards. The comparison shows that the Al^{3+} additives slightly contract the lattice volume of both phases. Given the smaller ionic radius of Al^{3+} vs. that of Ni^{2+} and Ni^{3+}, the lattice contraction supports that the Al^{3+} ions substitute for Ni ions in *P3*-$Na_{2/3}Ni_{1/2}Mn_{1/2}O_2$ and *P2*-$Na_{2/3}Ni_{1/3}Mn_{2/3}O_2$. Furthermore, the lattice volume of the *P2* phase shows a tendency to decrease after the oxide annealing from 800 to 900 °C. Compared with Al additives, the annealing temperature has a gentler effect on the layered structure. Although the Al^{3+} provokes a transformation from a *P3*- to a *P2*-type structure, the annealing temperature leads to a slight lattice volume compression.

Table 1. Lattice parameters of *P3* and *P2* phases for $Na_{2/3}Ni_{1/2-x}Al_xMn_{1/2}O_2$ (x = 0.08) annealed at 700, 800, and 900 °C. XRD-evaluated amount of *P3* and *P2* phases is expressed in weight %. For the sake of comparison, the lattice parameters for unsubstituted *P3*-$Na_{2/3}Ni_{1/2}Mn_{1/2}O_2$ and *P2*-$Na_{2/3}Ni_{1/3}Mn_{2/3}O_2$ are also given.

Samples	Structure	a, Å	c, Å	V, Å³	wt. %
P3-$Na_{2/3}Ni_{1/2}Mn_{1/2}O_2$ 700 °C	*P3*	2.8890	16.7230	120.88	
x = 0.08, 700 °C	*P3*	2.8890	16.7230	120.88	88
	P2	2.8905	11.1254	80.49	12
x = 0.08, 800 °C	*P2*	2.8903	11.0865	80.21	
x = 0.08, 900 °C	*P2*	2.8888	11.0986	80.20	
P2-$Na_{2/3}Ni_{1/3}Mn_{2/3}O_2$ 900 °C	*P2*	2.8889	11.1562	80.63	

The distribution of Al^{3+} into *P3* and *P2* phases is examined by EPR spectroscopy. Figure 2A compares the EPR spectra of the oxides annealed at 700, 800 and 900 °C, as well as *P3*-$Na_{2/3}Ni_{1/2}Mn_{1/2}O_2$ and *P2*-$Na_{2/3}Ni_{1/3}Mn_{2/3}O_2$ as references for the Ni-Mn magnetic systems. The EPR spectra of the layered reference oxides consist of a single Lorentzian line due to the two-dimensional magnetic interactions between the $Ni^{2+/3+}$ and Mn^{4+} ions inside the layers [36]. The magnetically coupled ions provoke a strong temperature dependence of the EPR parameters. Both the g-factor and EPR line width decrease with cooling from 400 to 80 K (Figure 2B). The different strengths of the magnetic interactions between the Ni and Mn ions in the *P3* and *P2* phases enable their differentiation with respect to the EPR line width: *P3*-$Na_{2/3}Ni_{1/2}Mn_{1/2}O_2$ has a broader EPR signal than that of *P2*-$Na_{2/3}Ni_{1/3}Mn_{2/3}O_2$ (i.e., 140 mT vs. 131 mT at 450 K).

The insertion of Al^{3+} into *P3*-$Na_{2/3}Ni_{1/2}Mn_{1/2}O_2$ and *P2*-$Na_{2/3}Ni_{1/3}Mn_{2/3}O_2$ proceeds without changing the EPR line shape, as well as the temperature dependence of the g-factor. This shows that the Ni-Mn spin system gives rise to the EPR spectra for the Al-substituted oxides too. The only parameter that is changed after Al^{3+} insertion is the EPR line width. For the Al-substituted oxide annealed at 700 °C (which is a mixture of the main *P3* phase and the impurity *P2* phase in the ratio of 88:12 wt. %), the EPR line width is narrowed in comparison to that of the unsubstituted *P3*-$Na_{2/3}Ni_{1/2}Mn_{1/2}O_2$. The line narrowing reflects a dilution of the Ni-Mn spin system due to the replacement of

paramagnetic Ni ions with diamagnetic Al^{3+} ions. This is in agreement with the XRD data, where a smaller lattice volume is observed for the Al-substituted *P3* phase. In addition, the effect of a small amount of the *P2* phase (having narrower line width) on the EPR line width cannot be discarded.
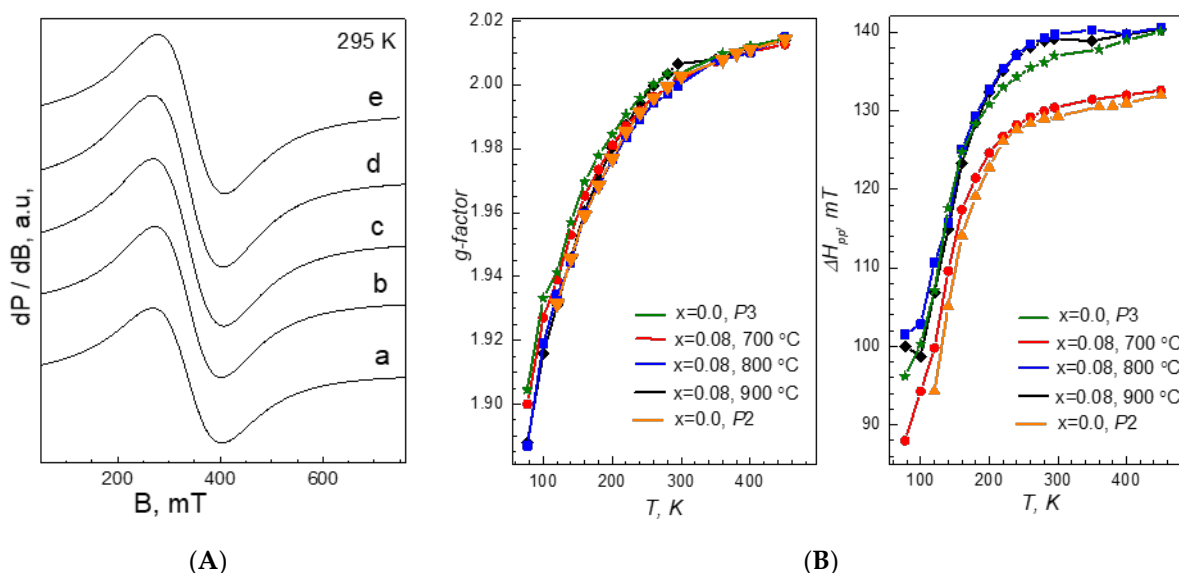

Figure 2. (**A**) EPR spectra of Al-substituted oxides annealed at 700 (b), 800 (c) and 900 °C (d) and reference oxides *P3*-$Na_{2/3}Ni_{1/2}Mn_{1/2}O_2$ (a) and *P2*-$Na_{2/3}Ni_{1/3}Mn_{2/3}O_2$ (e). (**B**) Temperature dependence of the g-factor and EPR line width (ΔHpp) for *P3*-$Na_{2/3}Ni_{1/2}Mn_{1/2}O_2$, *P2*-$Na_{2/3}Ni_{1/3}Mn_{2/3}O_2$ and Al-substituted oxides annealed at 700, 800 and 900 °C.

For the Al-substituted oxides annealed at 800 and 900 °C and containing a single *P2* phase, the EPR signal has the same line width, which is broader than that of the unsubstituted *P2*-$Na_{2/3}N_{1/3}Mn_{2/3}O_2$. At first glance, this is in contradiction to the dilution of the Ni-Mn spin system after Al^{3+} insertion. However, the simple substitution model does not take into account the cationic distribution inside the layers. For *P2*-$Na_{2/3}N_{1/3}Mn_{2/3}O_2$, it has been found that Ni^{2+} and Mn^{4+} ions are ordered so that every Ni^{2+} is surrounded by Mn^{4+}, and every Mn^{4+} has 3 Ni^{2+} and 3 Mn^{4+} [32]. This pattern of ordering ensures the maximum number of contacts between Ni^{2+} and Mn^{4+} via a common O, which in turn favors the development of effective Ni-Mn magnetic interactions. As a result, the EPR line width adopts the lowest value. The replacement of Ni by Al^{3+} appears to destroy the in-layer Ni-Mn cationic ordering, thus contributing to line broadening. The lack of Ni-Mn cationic ordering in Al-substituted oxides can be related to XRD patterns, where there is no peak at around 22°, which is typical for in-plane cationic ordering (Figure 1).

The next parameter that is changed after Al insertion is morphology (Figure 3). At 700 °C, large and irregular aggregates are formed. This type of morphology is typical for the layered oxides obtained by the thermal decomposition of organic-containing precursors [34]. The peculiarities in the oxide morphology are observed after their annealing above 700 °C. By increasing the annealing temperature from 700 to 800 °C, the individual particles begin to crystallize, adopting a plate-like shape and tending to stick together via common faces into column-like aggregates (Figure 3). In addition to plate-like particles, smaller and irregular particles are also visible. Further annealing of the oxide at 900 °C favors the growth of both plate-like and irregular particles, resulting in the disturbance of the column-like aggregates. The comparison indicates that, at 800 °C, the plate-like particles possess dimensions of around 1.0–2.0 μm in length and 0.1–0.3 μm in thickness, while at 900 °C, the particles become thicker (i.e., around 0.5 μm) without significantly changing their length (around 2.0 μm). In synchrony with the plate-like particles, the irregular particles also increase their dimensions from about 100 nm to 500 nm after enhancing the annealing temperature from

800 to 900 °C. It is worth mentioning that, at the same annealing temperature of 900 °C, the unsubstituted oxide having a *P2* structure displays better-crystalized particles with larger dimensions: an average length of 2–3 μm and a thickness of around 0.5–0.6 μm.
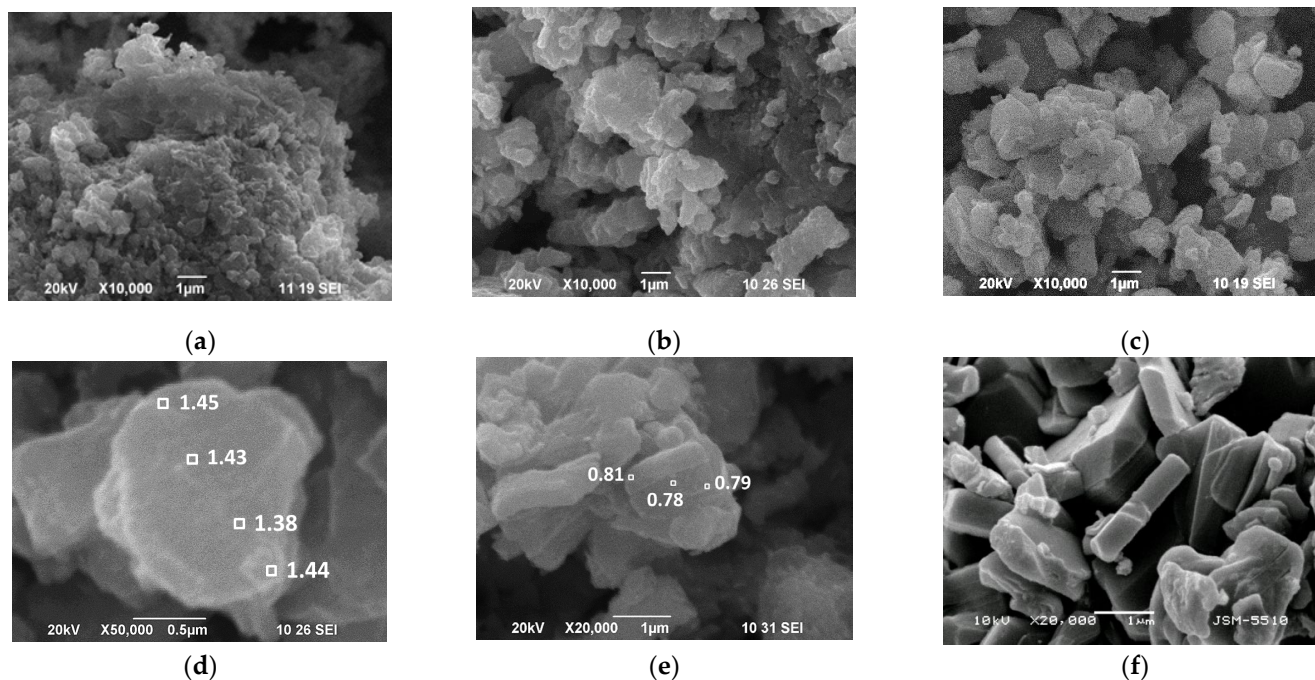

Figure 3. SEM images of Al-substituted oxides annealed at 700, 800 and 900 °C (**a–c**). SEM images with a high-resolution for Al-substituted oxides annealed at 800 and 900 °C (**d,e**) and *P2*-$Na_{2/3}Ni_{1/3}Mn_{2/3}O_2$ annealed at 900 °C (**f**). The box indicates the Al content (expressed in wt. %) determined by SEM-EDS analysis.

The primary particles are monitored by TEM (Figure 4). For the oxide annealed at 700 °C, well-crystallized particles with sizes between 200 and 500 nm are formed. SAED demonstrates that particles contain separate phases with a *P3* and *P2* structure, which is in accordance with XRD analysis (Figure 1b). This reveals that Al substitution proceeds through the formation of distinct *P2* and *P3* phases, and there is no intergrowth between them. After the enhancement of the annealing temperature from 700 to 800 °C, the particles retain their shapes and sizes, and the main phase crystallizes in the *P2*-type structure. This supports once again the transformation of the *P3* into the *P2* structure after annealing at 800 °C. A close examination of the TEM images for the oxide annealed at 800 °C discloses that the particles are stacked along the common faces, as observed in the SEM images (Figures 3b,d and 4b). Any attempt to take HR-TEM images shows that the lattice fringes corresponding to d_{001} and d_{002} for the *P2* structure, as well as to d_{003} for the *P3* structure (which is indistinguishable from d_{002} for the *P2* structure), are systematically lower than those determined from the X-ray diffraction experiments: 0.99 vs. 1.11 nm and 0.49 vs. 0.56 nm, respectively. This interlayer instability could be related to a well-known effect, according to which electron beam irradiation might induce a local temperature variation inside the particles during the HR-TEM experiment. This means that the Al-substituted oxides are unstable under electron beam irradiation, and they undergo some lattice compression. The compactness of the layered structure is also observed after increasing the annealing temperature from 700 to 900 °C (Table 1). This is an interesting finding that requires further examination.
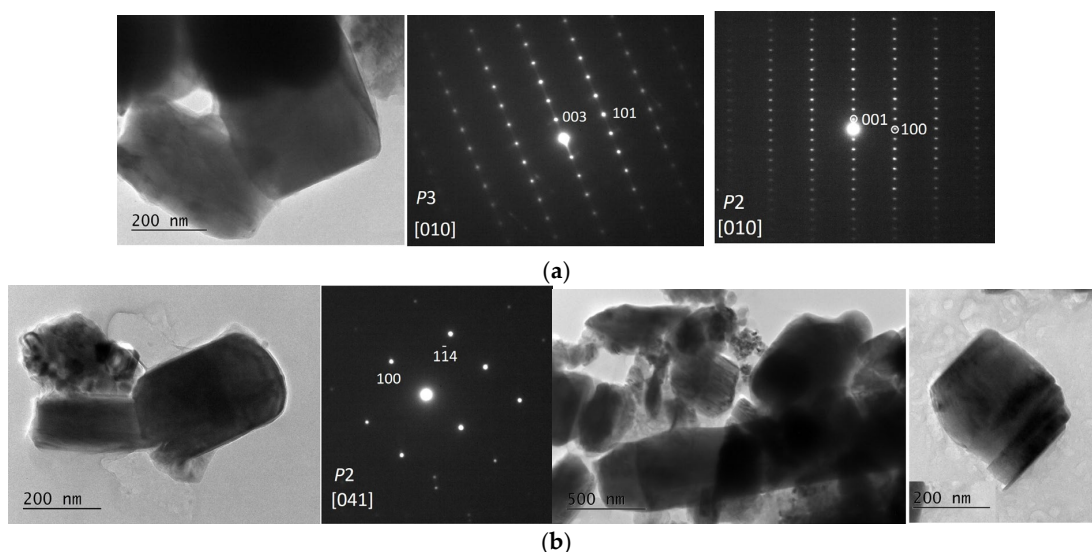
(**a**)

(**b**)

Figure 4. Bright-field images and SAED for Al-substituted oxides annealed at 700 °C (**a**) and 800 °C (**b**). The indexation of the electron diffraction is indicated.

3.2. Treatment of Layered Oxides with Al_2O_3

Given the phase composition of the Al-substituted oxides, the samples with a *P3* and *P2* structure are selected for the treatment with alumina. These are pristine $Na_{2/3}Ni_{1/2}Mn_{1/2}O_2$ with a *P3*-type structure and Al-substituted $Na_{2/3}Al_{0.08}Ni_{0.42}Mn_{0.50}O_2$ with a *P2*-type structure. The procedure includes the treatment of layered oxides with aluminum acetate, followed by thermal annealing at 700 °C for the pristine oxide and 800 °C for the Al-substituted oxide. After Al_2O_3 treatment, both the *P3* and *P2* structures are preserved, with the lattice parameters of *P3*-$Na_{2/3}Ni_{1/2}Mn_{1/2}O_2$ and *P2*-$Na_{2/3}Al_{0.08}Ni_{0.42}Mn_{0.50}O_2$ being the same (Figure 5). The close examination of XRD patterns of the treated oxides reveals the appearance of low-intensity peaks due to $NaAlO_2$. However, one can take into account that the thermal decomposition of the aluminum acetate at 700 and 800 °C results in the formation of amorphous aluminum oxide (Figure 5). Based on these data, it appears that, during the decomposition, one part of the aluminum acetate interacts with the surface of the layered oxides, yielding a separate phase of $NaAlO_2$ without affecting the oxide bulk, while the other part gives rise to the formation of amorphous aluminum oxide.
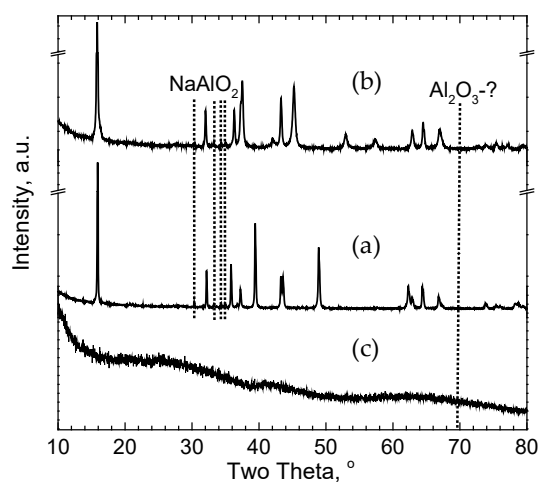

Figure 5. XRD patterns of Al_2O_3-treated *P3*-$Na_{2/3}Ni_{1/2}Mn_{1/2}O_2$ (**a**) and *P2*-$Na_{2/3}Al_{0.08}Ni_{0.42}Mn_{0.50}O_2$ (**b**). The XRD pattern of Al_2O_3 obtained at 800 °C after the thermal decomposition of Al acetate is also shown (**c**).

The morphology of the Al-treated oxides retains its main features (Figure 6). For the *P3* phase treated at 700 °C with alumina, there are large and irregular aggregates, which are composed of closely bonded individual particles with sizes of around 0.3 μm. The same picture is observed for the untreated *P3* phase [34]. For the *P2* phase treated at 800 °C, the typical column-like aggregates are also distinguished (Figure 6), as in the case of pristine $P2$-$Na_{2/3}Al_{0.08}Ni_{0.42}Mn_{0.50}O_2$ (Figure 3). To analyze the distribution of Al along the aggregates, SEM-EDS analysis is undertaken (Figures 3 and 6). The results evidence the uneven distribution of aluminum for both the *P3* and *P2* phases. For the Al-treated $P2$-$Na_{2/3}Al_{0.08}Ni_{0.42}Mn_{0.50}O_2$, the Al content is higher for the regions composed of small particles (i.e., sizes less than 100 nm), while the regions containing mainly plate-like particles display lower Al content. It is of importance that the Al content of the plate-like particles is slightly higher than that determined for the plate-like particles of the untreated oxide: 2.1 ± 0.4 wt. % vs. 1.5 ± 0.3 wt. % (Figures 3 and 6). The SEM data disclose that the Al treatment of the layered oxide leads to a concentration of Al on the smaller particles, while the plate-like particles slightly accommodate alumina.
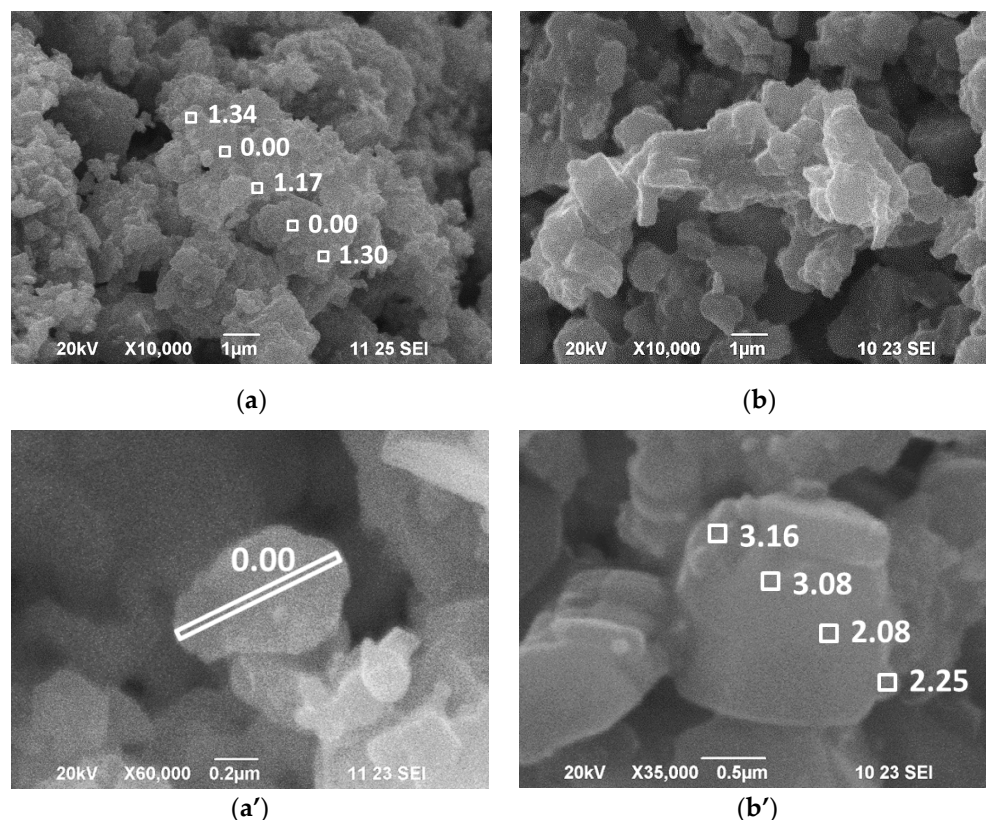

Figure 6. SEM images of Al_2O_3-treated $P3$-$Na_{2/3}Ni_{1/2}Mn_{1/2}O_2$ (**a,a′**) and $P2$-$Na_{2/3}Al_{0.08}Ni_{0.42}Mn_{0.50}O_2$ (**b,b′**). The box indicates the Al content (expressed in wt. %) determined by SEM-EDS analysis.

3.3. Na Storage Performance of Al-Substituted and Al_2O_3-Treated Layered Oxides

Figures 7–9 compare the CV curves for the Al-substituted oxides and those of unsubstituted *P3* and *P2* phases. The comparison enables outlining two features. First, the *P3* and *P2* phases display the same CV curve profiles, as previously found [34] (Figure 7). After the first anodic and consecutive cathodic scan, two types of peaks dominate the CV curves: low-voltage peaks between 3.0 and 3.8 V and high-voltage peaks between 3.8 and 4.5 V. The anodic peaks observed at 4.75 V for the *P3* phase and above 4.5 V for the *P2* phase most probably come from the decomposition of the electrolyte. The low-voltage peaks at 3.50 and 3.85 V reflect the oxidation and reduction of Ni ions occurring during partial Na^+ extraction and insertion, as previously established. At a potential of 4.0 V, the extraction of 1/3 of Na^+ leads to the monoclinic distortion of the *P3* phase (i.e., $Na_{\sim0.3}Ni_{1/2}Mn_{1/2}O_2$), while

this process results in a strong change in the lattice parameters in the framework of the *P2* structure for Na$_{\sim0.3}$Ni$_{1/3}$Mn$_{2/3}$O$_2$ [34,36,37]. The origin of the high-voltage peak around 4.4 V is more complex. For the *P3* phase, the peak at 4.34 V corresponds to the complete extraction of Na$^+$ concomitant with the oxidation of nickel ions and lattice oxygen [7,37], while for the *P2* phase, the complete extraction of Na$^+$ proceeds at 4.34 V together with a structural transformation from the *P2* to the *O2* type and a strong interlayer space contraction (more than 20%) [38]. This structural transition determines the poor cycling stability of *P2*-Na$_{2/3}$Ni$_{1/3}$Mn$_{2/3}$O$_2$ in the extended voltage range [2]. The poor performance of the *P2* phase is well demonstrated by the CV curves after the five anodic and cathodic scans. Although the low-voltage peaks remain almost unchanged, the high-voltage peak diminishes significantly. On the contrary, the high-voltage peak appears more stable for the *P3* phase, which is a consequence of the restoration of the *P3* structure after the complete extraction of Na$^+$ [35]. The additional peak at 2.2/1.7 V corresponds, most probably, to the oxidation of Mn ions instead of the Ni ones. This process is also similar for both the *P3* and *P2* phases.
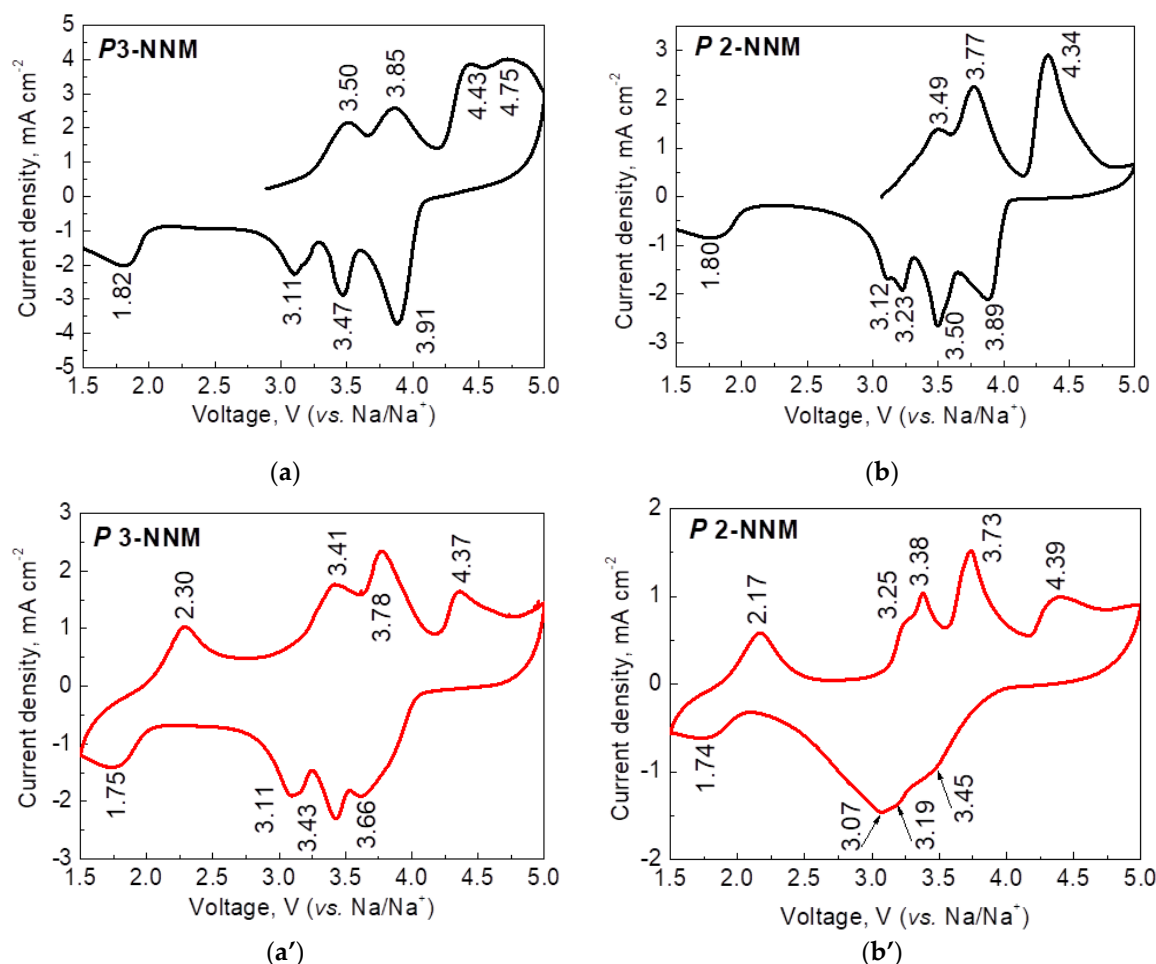

Figure 7. CV curves after the 1st and 5th scans for *P3*-Na$_{2/3}$Ni$_{1/2}$Mn$_{1/2}$O$_2$ (*P3*-NNM—**a,a′**) and *P2*-Na$_{2/3}$Ni$_{1/3}$Mn$_{2/3}$O$_2$ (P2-NNM, **b,b′**).

Second, the Al additives do not influence the oxidation and reduction peaks in the CV curves (Figure 8). This indicates the preservation of the mechanism of the electrochemical reaction after the Al substitution of Ni in the layered oxides. For the layered oxides treated with Al$_2$O$_3$, the CV curves also retain their profiles (Figure 9). The insensitivity of the redox peaks from the Al additives and Al$_2$O$_3$ modifiers can be related to the electrochemical reaction taking place in the layered oxides. The insertion and extraction of Na$^+$ are

concomitant with the redox activity of Ni ions and lattice oxygen, which are common for all oxides. However, a close inspection of the CV curves reveals some peculiarities for the Al-substituted and Al_2O_3-treated oxides. These peculiarities are associated with the high-voltage peak after the five cathodic and anodic scans. The comparison shows that the high-voltage peak is better resolved for the Al-substituted and Al_2O_3-treated oxides than those of the unsubstituted *P3*-$Na_{2/3}Ni_{1/2}Mn_{1/2}O_2$ and *P2*-$Na_{2/3}Ni_{1/3}Mn_{2/3}O_2$. The stabilization of the high-voltage peak is a prerequisite for the improved electrochemical performance of the Al-substituted and Al_2O_3-treated oxides.
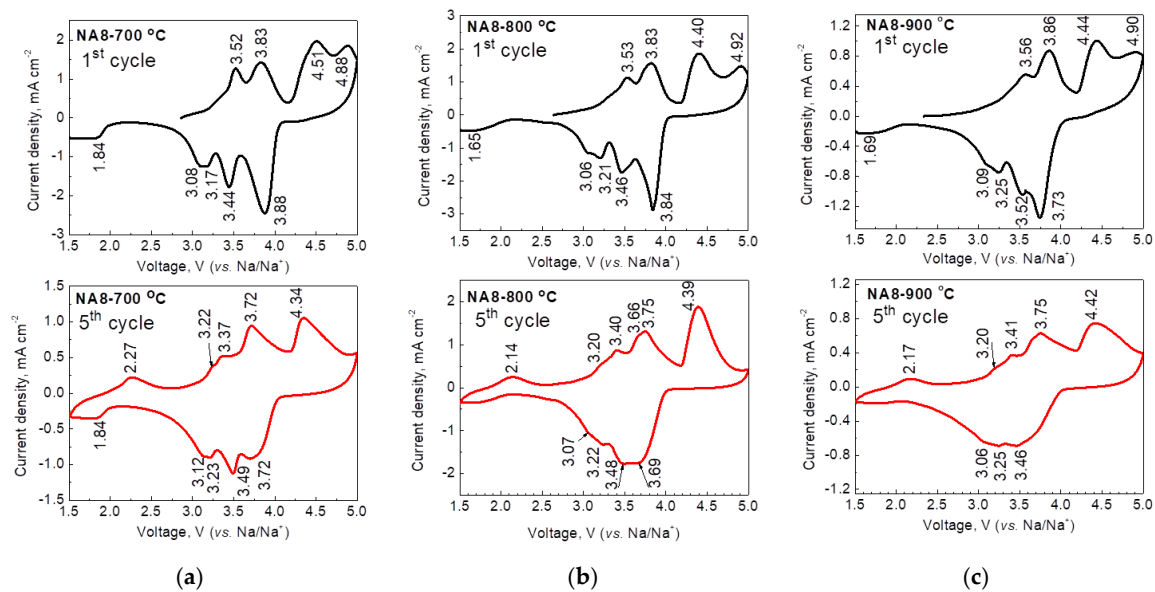

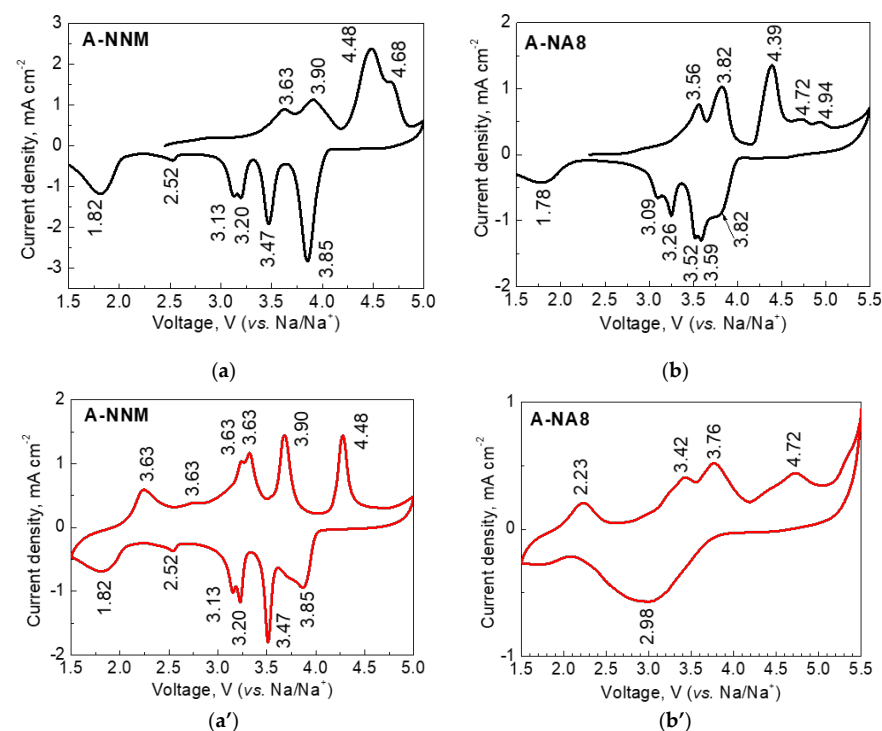**Figure 8.** CV curves after the 1st and 5th scans for Al-substituted oxides annealed at 700, 800 and 900 °C (**a**–**c**).

Figure 9. CV curves after the 1st and 5th scans for Al_2O_3-treated *P3*-$Na_{2/3}Ni_{1/2}Mn_{1/2}O_2$ annealed at 700 °C (**a**,**a′**) and Al_2O_3-treated *P2*-$Na_{2/3}Ni_{0.42}Al_{0.08}Mn_{1/2}O_2$ annealed at 800 °C (**b**,**b′**).

To verify this suggestion, the cycling stability of Al-substituted oxides is compared in Figure 10. The electrochemical test is carried out in two potential ranges: in a narrow range between 1.5 and 4.2 V and in a broad potential range between 1.5 and 4.8 V, where the proceeding of the high-voltage reaction is activated. In a narrow potential range, all Al-substituted oxides deliver nearly the same capacity, which varies between 60 and 70 mAh/g. The cycling stability is also comparable for all oxides: 17%, 15% and 24% after 100 cycles at a rate of C/2 for oxides annealed at 700, 800 and 900 °C, respectively. Contrary to the narrow potential range, the broad potential range enables a clear differentiation of the Al-substituted oxides. The highest capacity is delivered by the Al-substituted oxide annealed at 800 °C and having a *P2*-type structure, while the counterpart annealed at 900 °C delivers the smallest capacity. The Al-substituted oxide annealed at 700 °C and containing a phase mixture between *P3* and *P2* displays an intermediate capacity in comparison with that of the oxides annealed at 800 and 900 °C. The difference in the capacities of the Al-substituted oxides comes from the high-voltage peak, which is well demonstrated by the corresponding charge/discharge curves (Figure 11). Thus, the galvanostatic experiments support the concept of the stabilization of the high-voltage peak as a sign of the improved electrochemical performance of the Al-substituted oxides. To explain this effect, we measured the electrical resistivity of the substituted oxides. In comparison with the high-voltage peak, the electrical resistivity of Al-substituted oxides is relatively comparable (i.e., the values vary around $2–5 \times 10^6$ Ohm.cm at 470 K without any clear dependence on the structure type and oxide annealing temperature). In addition, the lack of intergrowth between the *P3* and *P2* phases (Figure 4) cannot also explain the observed stabilization of the high-voltage peak, as has been discussed in previous reports [39,40]. This means that the stabilization of the high-voltage peak is not a simple consequence of the replacement of Ni by Al.

When $P3$-$Na_{2/3}Ni_{1/2}Mn_{1/2}O_2$ is treated with Al_2O_3, the capacity increases from 120 to around 150 mAh/g, but the capacity stability remains comparable with that of the untreated oxide (Figure 10). This is not the case when $P2$-$Na_{2/3}Ni_{0.42}Al_{0.08}Mn_{1/2}O_2$ is treated with Al_2O_3, with the capacity and cycling stability being unchanged. The difference between the Al_2O_3-treated $P3$ and $P2$ oxides can be related to the high-voltage peak. $P2$-$Na_{2/3}Ni_{0.42}Al_{0.08}Mn_{1/2}O_2$ displays a well-resolved high-voltage peak before its treatment with Al_2O_3, while the high-voltage peak becomes visible only after the treatment of $P3$-$Na_{2/3}Ni_{1/2}Mn_{1/2}O_2$ with Al_2O_3 (Figures 9 and 10). The results underline once again the concept of the relationship between the high-voltage peak, capacity and capacity stability. The better the resolution of the high-voltage peak, the greater the capacity and the superior the cyclic stability.

Further insight into the cycling stability of layered oxides is provided by ex situ EPR spectroscopy (Figure 12). The EPR spectra of the cycled oxides show a Lorentzian line, whose line width increases dramatically for the Al-substituted oxides annealed at 700 and 900 °C (more than 20 mT, Table 1). On the contrary, for the cycled Al-substituted oxide annealed at 800 °C, the EPR line width tends to be that of the pristine oxide. It is important that line broadening proceeds without changing the g-factor of the EPR signal, thus indicating the preservation of the Ni-Mn spin system during oxide cycling. Therefore, EPR line broadening can be interpreted in terms of cationic reorganization occurring during the electrochemical reaction. One of the possible cationic reorganization processes includes the well-known reaction of transition metal ion migration initiated during the complete extraction of Na+ from layered oxides [16,41]. Cationic migration has been shown to be responsible for the cycling performance of layered oxides when they are charging/discharging in a wide potential range [16,41]. Among the transition metal ions, nickel, iron and magnesium ions display a strong tendency to migrate toward the depleted Na+ layers, while manganese and cobalt ions remain in their crystallographic positions [16,41]. This causes a structural evolution, which contributes to the worse cycling stability of layered oxides [41]. Returning to the samples we studied, the retention of the EPR line width during oxide cycling is a sign that the cationic migration is a reversible process for the oxide

annealed at 800 °C. This oxide is characterized by the best cycling stability. On the contrary, for the oxides annealed at 700 and 900 °C, the cationic migration appears to be a partially reversible process, which leads to a structural degradation expressed in the broadening of the EPR signal. As a result, both oxides exhibit worse cycling stability.
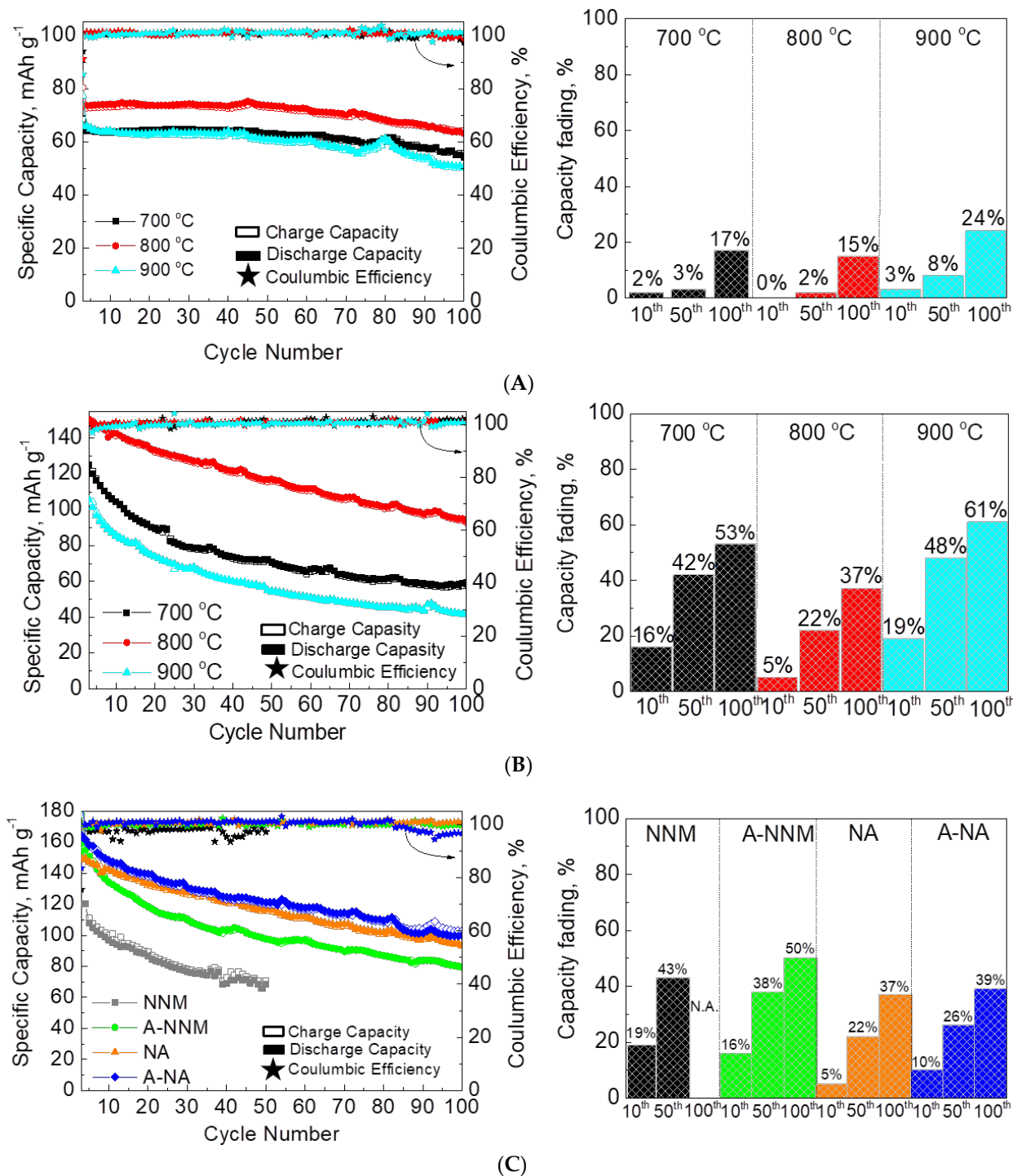

(**A**)

(**B**)

(**C**)

Figure 10. Cycling stability and Coulombic efficiency (left) of Al-substituted oxides annealed at 700, 800 and 900 °C in two voltage ranges: 1.5–4.2 V (**A**) and 1.5–4.8 V (**B**). Cycling stability and Coulombic efficiency of Al_2O_3-treated *P3*-$Na_{2/3}Ni_{1/2}Mn_{1/2}O_2$ annealed at 700 °C (A-NNM) and Al_2O_3-treated *P2*-$Na_{2/3}Ni_{0.42}Al_{0.08}Mn_{1/2}O_2$ annealed at 800 °C (A-NA) in the voltage range of 1.5–4.8 V (**C**). The charging rate is C/2. The capacity fading for the 10th, 50th and 100th cycles is shown on the right.
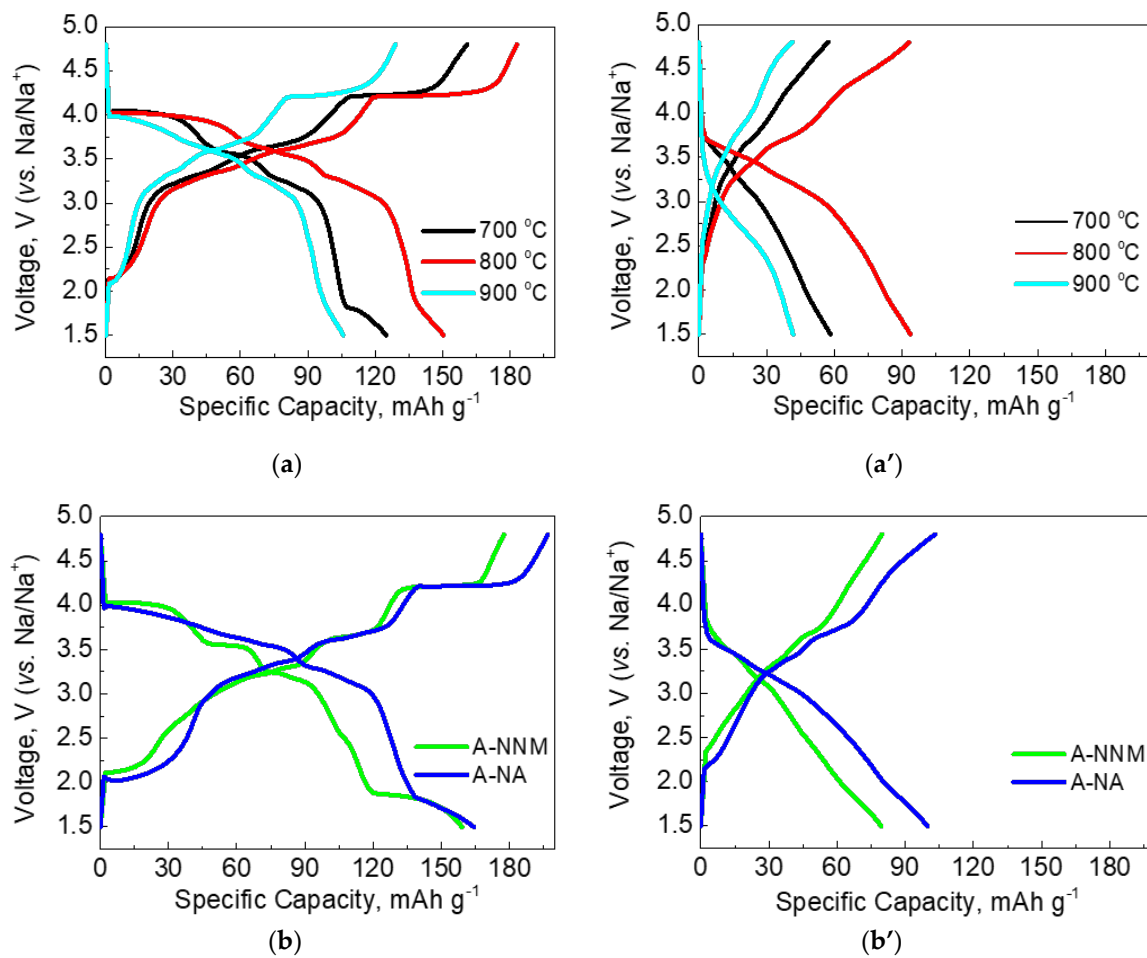
Figure 11. Charge/discharge curves after 1st and 100th cycles for Al-substituted oxides annealed at 700, 800 and 900 °C (**a**,**a′**), as well as Al_2O_3-treated *P3*-$Na_{2/3}Ni_{1/2}Mn_{1/2}O_2$ annealed at 700 °C and Al_2O_3-treated *P2*-$Na_{2/3}Ni_{0.42}Al_{0.08}Mn_{1/2}O_2$ annealed at 800 °C. The charging rate is C/2 (**b**,**b′**).

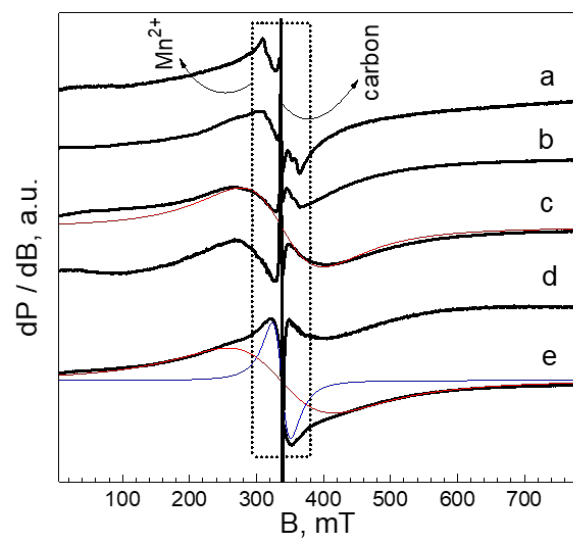**Figure 12.** Ex situ EPR spectra of oxide electrodes cycled between 1.5 and 4.8 V for 100th cycles: (**a**) *P3*-$Na_{2/3}Ni_{1/2}Mn_{1/2}O_2$; (**b**) Al_2O_3-treated *P3*-$Na_{2/3}Ni_{1/2}Mn_{1/2}O_2$; (**c**) $Na_{2/3}Ni_{0.42}Al_{0.08}Mn_{1/2}O_2$ annealed at 700 °C; (**d**) $Na_{2/3}Ni_{0.42}Al_{0.08}Mn_{1/2}O_2$ annealed at 800 °C; (**e**) $Na_{2/3}Ni_{0.42}Al_{0.08}Mn_{1/2}O_2$ annealed at 900 °C. The signals due to Mn^{2+} ions and carbon additives are indicated.

The question is why cationic migration is a reversible process for the oxide annealed at 800 °C only. This can be related to the oxide morphology, which contributes to the improvement in cationic migration kinetics. It seems that the reaction kinetics are facilitated by the specific oxide morphology, which comprises plate-like particles stacked via common faces into column-like aggregates (Figure 3). This interesting finding needs further examination in order to design more-efficient electrode materials.

For the oxides treated with Al_2O_3, there is no clear dependence of the EPR line width upon oxide cycling (Table 2). However, even in this case, the EPR spectroscopy allows differentiating the pristine oxide and Al_2O_3-treated oxides with respect to their cycling stability (Figure 12). In addition to the broad signal, a new sextet signal is detected for the cycled oxides. This signal is characterized by a g-factor of 2.002 and a hyperfine constant of 90 mT (Figure 12). Based on previous literature data [42], the sextet signal is assigned to Mn^{2+} ions surrounded by F^- ions. The origin of the sextet signal can be related to an "electrode–electrolyte" interaction. It is well accepted that Mn-rich layered oxides undergo a severe Mn^{2+} dissolution in carbonate-based electrolytes due to the disproportion of Mn^{3+} into Mn^{2+} and Mn^{4+} [43]. Recently, the dissolution of nickel and cobalt ions from oxide-based cathodes has also been detected and discussed for conventional $LiCoO_2$ and Ni-rich and oxides [44,45]. Through EPR spectroscopy, it appears that dissolved Mn^{2+} ions in the electrolyte are re-deposited on the electrode surface as fluoride complexes. Deposed MnF_2 has been shown to play a twofold role: on the one hand, it passivates the electrode surface, thus preventing further interaction with the electrolyte and its decomposition; on the other hand, it impedes the alkali ion transfer from the oxide surface into the bulk [7,28]. Through EPR, we detected only the signal due to MnF_2 and any signal due to Ni-fluoride complexes. However, the different sensitivity of the EPR spectroscopy in the X-band toward Mn^{2+} and Ni^{2+} ions should be taken into account. Therefore, the deposition of NiF_2 on the electrode surface cannot be rejected.

Table 2. EPR line width for Al-substituted and Al_2O_3-treated oxide electrodes after 100 cycles at a charge rate of C/2.

Samples	T = 295 K		T = 100 K	
	Pristine Oxide, ΔHpp (mT)	Cycled Oxide, ΔHpp (mT)	Pristine Oxide, ΔHpp (mT)	Cycled Oxide, ΔHpp (mT)
Al-substituted oxide annealed at 700 °C (x = 0.08)	130	137	94	117
Al-substituted oxide annealed at 800 °C (x = 0.08)	140	146	103	110
Al-substituted oxide annealed at 900 °C (x = 0.08)	140	158	99	123
Al_2O_3-treated oxide, annealed at 700 °C	130	139	95	105
Al_2O_3-treated Al-substituted oxide, annealed at 800 °C	137	142	98	104

The comparison of the EPR spectra demonstrates that the most intensive sextet signal is detected for $P3$-$Na_{2/3}Ni_{1/2}Mn_{1/2}O_2$, while for Al_2O_3-treated $P3$-$Na_{2/3}Ni_{1/2}Mn_{1/2}O_2$, the sextet signal is hardly visible. The same picture is observed for Al_2O_3-treated $P2$-$Na_{2/3}Ni_{0.42}Al_{0.08}Mn_{1/2}O_2$ (not shown). This means that Mn dissolution is suppressed for the Al_2O_3-treated oxides.

In comparison with the Al_2O_3-treated oxides, the Al-substituted oxides display a more complex picture, especially for the oxide annealed at 900 °C. Although the Al-substituted oxides annealed at 700 and 800 °C display only one broad signal, the EPR spectrum of the annealed oxide at 900 °C can be deconvoluted by at least of two signals: a broad signal due to the Ni-Mn spin systems of layered oxides and a narrow signal. The EPR parameters of the narrow signal are a g-factor of 2.002 and an EPR line width of 26 mT. These EPR parameters permit attributing the narrow signal to Mn^{2+} ions in Mn-F complexes too. In this case, the merge of the sextet signal into one single envelope is induced by the increased concentration of Mn^{2+} ions deposed on the surface of the oxide annealed at 900 °C: the higher the concentration of Mn^{2+} ions, the stronger the magnetic interactions

(both dipole–dipole and exchange interactions), which, in turn, leads to a coalesce of the sextet lines [36]. This means that the oxide annealed at 900 °C suffers from strong Mn dissolution in the NaPF$_6$-based electrolyte, which yields a capacity degradation upon cycling (Figure 10B).

4. Conclusions

Layered sodium nickel manganese oxide displays a limited ability to accommodate aluminum in its structure (i.e., up to 8 at. %). Aluminum substitution of Ni in Na$_{2/3}$Ni$_{1/2}$Mn$_{1/2}$O$_2$ facilitates the stabilization of *P2* structural modification and provokes the disordering of Ni and Mn ions inside the layers. The oxide annealed at 800 °C exhibits a *P2*-type structure with a specific morphology consisting of column-like aggregates of stacked plate-like primary particles along the face. The impregnation of pristine *P3*-Na$_{2/3}$Ni$_{1/2}$Mn$_{1/2}$O$_2$ and Al-substituted *P2*-Na$_{2/3}$Al$_{0.08}$Ni$_{0.42}$Mn$_{0.50}$O$_2$ with aluminum acetate leads to the formation of composites between layered oxides and Al$_2$O$_3$ without affecting their layered structure and morphology.

The Na$^+$ extraction/insertion into Al-substituted and Al$_2$O$_3$-treated oxides proceeds thanks to the redox reactions of nickel and oxygen ions, and it is insensitive toward layer stacking. The Al substituents and Al$_2$O$_3$ modifiers contribute to the stabilization of the high-voltage peak at 4.4 V, thus resulting in the enhancement of the capacity. During the cycling of tAl-substituted oxides, a cationic reconstruction including mainly cationic migration between layers takes place. The reversibility of the cationic migration depends on the oxide morphology; for the oxide with stacked plate-like particles, the migration becomes a reversible process. The treatment of layered oxides with Al$_2$O$_3$ mitigates the Mn dissolution reaction occurring during electrode cycling in the NaPF$_6$-based electrolyte. Mn dissolution followed by the reverse deposition of MnF$_2$ on the electrode surface is the most intensive process for the Al-substituted oxide annealed at 900 °C.

Based on the established relationships between structure and surface modifications, the best electrode was selected. This is an Al-substituted oxide, *P2*-Na$_{2/3}$Ni$_{0.42}$Al$_{0.08}$Mn$_{1/2}$O$_2$, annealed at 800 °C; thanks to the Al additives and specific column-like morphology, the high-voltage redox reaction is facilitated together with suppression of the Mn dissolution of the oxide in the electrolyte, enhancing the reversibility of the cationic migration between layers. As a result, the oxide *P2*-Na$_{2/3}$Ni$_{0.42}$Al$_{0.08}$Mn$_{1/2}$O$_2$ is resistant in a broad potential range and delivers a capacity of around 110 mAh/g at a rate of C/2 after 100th cycles.

This study demonstrates how the manipulation of the high-voltage reaction, cationic migration between layers and Mn dissolution through Al substitution and Al$_2$O$_3$ treatment enable designing high-performance electrode materials for sodium-ion batteries.

Conflicts of Interest: The authors declare no conflict of interest.

References

1. Liu, T.; Zhang, Y.; Jiang, Z.; Zeng, X.; Ji, J.; Li, Z.; Gao, X.; Sun, M.; Lin, Z.; Ling, M.; et al. Exploring competitive features of stationary sodium ion batteries for electrochemical energy storage. *Energy Environ. Sci.* **2019**, *12*, 1512–1533. [CrossRef]
2. Hirsh, H.S.; Li, Y.; Tan, D.H.S.; Zhang, M.; Zhao, E.; Meng, Y.S. Sodium-Ion Batteries Paving the Way for Grid Energy Storage. *Adv. Energy Mater.* **2020**, *10*, 2001274. [CrossRef]
3. Su, H.; Jaffer, S.; Yu, H. Transition metal oxides for sodium-ion batteries. *Energy Storage Mater.* **2016**, *5*, 116–131. [CrossRef]
4. Wei, F.; Zhang, Q.; Zhang, P.; Tian, W.; Dai, K.; Zhang, L.; Mao, J.; Shao, G. Review—Research Progress on Layered Transition Metal Oxide Cathode Materials for Sodium Ion Batteries. *J. Electrochem. Soc.* **2021**, *168*, 050524. [CrossRef]
5. Liu, Q.; Hu, Z.; Li, W.; Zou, C.; Jin, H.; Wang, S.; Chou, S.; Dou, S.-X. Sodium transition metal oxides: The preferred cathode choice for future sodium-ion batteries? *Energy Environ. Sci.* **2021**, *14*, 158–179. [CrossRef]
6. Shi, C.; Wang, L.; Chen, X.; Li, J.; Wang, S.; Wang, J.; Jin, H. Challenges of layer-structured cathodes for sodium-ion batteries. *Nanoscale Horiz.* **2022**, *7*, 338–351. [CrossRef] [PubMed]
7. Kalapsazova, M.; Kukeva, R.; Zhecheva, E.; Stoyanova, R. Metal Substitution versus Oxygen-Storage Modifier to Regulate the Oxygen Redox Reactions in Sodium-Deficient Three-Layered Oxides. *Batteries* **2022**, *8*, 56. [CrossRef]
8. Chang, Y.-X.; Yu, L.; Xing, X.; Guo, Y.-J.; Xie, Z.; Xu, S. Ion Substitution Strategy of Manganese-Based Layered Oxide Cathodes for Advanced and Low-Cost Sodium Ion Batteries. *Chem. Rec.* **2022**, *10*, e202200122. [CrossRef] [PubMed]
9. Li, Y.; Chen, M.; Liu, B.; Zhang, Y.; Liang, X.; Xia, X. Heteroatom Doping: An Effective Way to Boost Sodium Ion Storage. *Adv. Energy Mater.* **2020**, *10*, 2000927. [CrossRef]
10. Kaufman, J.L.; Vinckevičiūtė, J.; Kolli, S.K.; Goiri, J.G.; Van der Ven, A. Understanding intercalation compounds for sodium-ion batteries and beyond. *Philos. Trans. A Math. Phys. Eng. Sci.* **2019**, *377*, 20190020. [CrossRef]
11. Zhang, X.; Yu, H.J. Crystalline Domain Battery Material. *Acc. Chem. Res.* **2020**, *53*, 368–379. [CrossRef] [PubMed]
12. Ma, Z.; Zhao, Z.; Xu, H.; Sun, J.; He, X.; Lei, Z.; Liu, Z.-H.; Jiang, R.; Li, Q. A Queue-Ordered Layered Mn-Based Oxides with Al Substitution as High-Rate and High-Stabilized Cathode for Sodium-Ion Batteries. *Small* **2021**, *17*, e2006259. [CrossRef] [PubMed]
13. Abate, I.; Kim, S.Y.; Pemmaraju, C.D.; Toney, M.F.; Yang, W.; Devereaux, T.P.; Chueh, W.C.; Nazar, L.F. The Role of Metal Substitution in Tuning Anion Redox in Sodium Metal Layered Oxides Revealed by X-Ray Spectroscopy and Theory. *Angew. Chem. Int. Ed.* **2021**, *60*, 10880–10887. [CrossRef] [PubMed]
14. Di Lecce, D.; Campanella, D.; Hassoun, J. Insight on the Enhanced Reversibility of a Multi-Metal Layered Oxide for Sodium-Ion Battery. *J. Phys. Chem. C* **2018**, *122*, 23925–23933. [CrossRef]
15. Singh, G.; Tapia-Ruiz, N.; del Amo, J.M.L.; Maitra, U.; Somerville, J.W.; Armstrong, A.R.; de Ilarduya, J.M.; Rojo, T.; Bruce, P.G. High Voltage Mg-Doped $Na_{0.67}Ni_{0.3-x}Mg_xMn_{0.7}O_2$ (x = 0.05, 0.1) Na-Ion Cathodes with Enhanced Stability and Rate Capability. *Chem. Mater.* **2016**, *28*, 5087–5094. [CrossRef]
16. Kalapsazova, M.; Markov, P.; Kostov, K.; Zhecheva, E.; Nihtianova, D.; Stoyanova, R. Controlling at Elevated Temperature the Sodium Intercalation Capacity and Rate Capability of $P3$-$Na_{2/3}Ni_{1/2}Mn_{1/2}O_2$ through the Selective Substitution of Nickel with Magnesium. *Batter. Supercaps* **2020**, *3*, 1329–1340. [CrossRef]
17. Wu, X.; Xu, G.-L.; Zhong, G.; Gong, Z.; McDonald, J.; Zheng, S.; Fu, R.; Chen, Z.; Amine, K.; Yang, Y. Insights into the effects of zinc doping on structural phase transition of $P2$-type sodium nickel manganese oxide cathodes for high-energy sodium ion batteries. *ACS Appl. Mater. Interfaces* **2016**, *8*, 22227–22237. [CrossRef]
18. Bai, X.; Sathiya, M.; Mendoza-Sanchez, B.; Iadecola, A.; Vergnet, J.; Dedryvere, R.; Saubanere, M.; Abakumov, A.M.; Rozier, P.; Tarascon, J.-M. Anionic Redox Activity in a Newly Zn-Doped Sodium Layered Oxide $P2$-$Na_{2/3}Mn_{1-y}Zn_yO_2$ (0 < y < 0.23). *Adv. Energy Mater.* **2018**, *8*, 1802379.
19. Wang, H.; Gao, R.; Li, Z.; Sun, L.; Hu, Z.; Liu, X. Different Effects of Al Substitution for Mn or Fe on the Structure and Electrochemical Properties of $Na_{0.67}Mn_{0.5}Fe_{0.5}O_2$ as a Sodium Ion Battery Cathode Material. *Inorg. Chem.* **2018**, *57*, 5249–5257. [CrossRef]
20. Cheng, C.; Ding, M.; Yan, T.; Jiang, J.; Mao, J.; Feng, X.; Chan, T.-S.; Li, N.; Zhang, L. Anionic Redox Activities Boosted by Aluminum Doping in Layered Sodium-Ion Battery Electrode. *Small Methods* **2022**, *6*, 2101524. [CrossRef]
21. Ramasamy, H.V.; Kaliyappan, K.; Thangavel, R.; Seong, W.M.; Kang, K.; Chen, Z.; Lee, Y.-S. Efficient Method of Designing Stable Layered Cathode Material for Sodium Ion Batteries Using Aluminum Doping. *J. Phys. Chem. Lett.* **2017**, *8*, 5021–5030. [CrossRef] [PubMed]
22. Soares, C.; Silvan, B.; Choi, Y.-S.; Celorrio, V.; Seymour, V.R.; Cibin, G.; Griffin, J.M.; Scanlon, D.O.; Tapia-Ruiz, N. $Na_{2.4}Al_{0.4}Mn_{2.6}O_7$ anionic redox cathode material for sodium-ion batteries—A combined experimental and theoretical approach to elucidate its charge storage mechanism. *J. Mater. Chem. A* **2022**, *10*, 7341–7356. [CrossRef]
23. Li, J.; Hu, H.; Wang, J.; Xiao, Y. Surface chemistry engineering of layered oxide cathodes for sodium-ion batteries. *Carbon Neutralization* **2022**, *1*, 96–116. [CrossRef]
24. Jung, S.C.; Kim, H.-J.; Choi, J.W.; Han, Y.-K. Sodium Ion Diffusion in Al2O3: A Distinct Perspective Compared with Lithium Ion Diffusion. *Nano Lett.* **2014**, *14*, 6559–6563. [CrossRef] [PubMed]
25. Zuo, W.; Qiu, J.; Liu, X.; Zheng, B.; Zhao, Y.; Li, J.; He, H.; Zhou, K.; Xiao, Z.; Li, Q.; et al. Highly-stable $P2$–$Na_{0.67}MnO_2$ electrode enabled by lattice tailoring and surface engineering. *Energy Storage Mater.* **2020**, *26*, 503–512. [CrossRef]

26. Hwang, J.-Y.; Myung, S.-T.; Choi, J.U.; Yoon, C.S.; Yashirod, H.; Sun, Y.-K. Resolving the degradation pathways of the O_3-type layered oxide cathode surface through the nano-scale aluminum oxide coating for high-energy density sodium-ion batteries. *J. Mater. Chem. A* **2017**, *5*, 23671–23680. [CrossRef]

27. Liu, Y.; Fang, X.; Zhang, A.; Shen, C.; Liu, Q.; Enaya, H.A.; Zhou, C. Layered *P2*-$Na_{2/3}[Ni_{1/3}Mn_{2/3}]O_2$ as high-voltage cathode for sodium-ion batteries: The capacity decay mechanism and Al_2O_3 surface modification. *Nano Energy* **2016**, *27*, 27–34. [CrossRef]

28. Kalapsazova, M.; Kostov, K.; Kukeva, R.; Zhecheva, E.; Stoyanova, R. Oxygen-Storage Materials to Stabilize the Oxygen Redox Activity of Three-Layered Sodium Transition Metal Oxides. *J. Phys. Chem. Lett.* **2021**, *12*, 7804–7811. [CrossRef]

29. Zhang, Q.; Gu, Q.-F.; Li, Y.; Fan, H.-N.; Luo, W.-B.; Liu, H.-K.; Dou, S.-X. Surface Stabilization of O_3-type Layered Oxide Cathode to Protect the Anode of Sodium Ion Batteries for Superior Lifespan. *Iscience* **2019**, *19*, 244–254. [CrossRef]

30. Feng, Y.-H.; Cheng, Z.; Xu, C.-L.; Yu, L.; Si, D.; Yuan, B.; Liu, M.; Zhao, B.; Wang, P.-F.; Han, X. Low-Cost Al-Doped Layered Cathodes with Improved Electrochemical Performance for Rechargeable Sodium-Ion Batteries. *ACS Appl. Mater. Interfaces* **2022**, *14*, 23465–23473. [CrossRef]

31. Nayak, D.; Jha, P.K.; Ghosh, S.; Adyam, V. Aluminium substituted β–type $NaMn_{1-x}Al_xO_2$: A stable and enhanced electrochemical kinetic sodium-ion battery cathode. *J. Power Sources* **2019**, *438*, 227025. [CrossRef]

32. Delmas, C.; Fouassier, C.; Hagenmuller, P. Structural Classification and Properties of the Layered Oxides. *Phys. B+C* **1980**, *99*, 81–85. [CrossRef]

33. Kalapsazova, M.; Zhecheva, E.; Tyuliev, G.; Nihtianova, D.; Mihaylov, L.; Stoyanova, R. Effects of the Particle Size Distribution and of the Electrolyte Salt on the Intercalation Properties of *P3*-$Na_{2/3}Ni_{1/2}Mn_{1/2}O_2$. *J. Phys. Chem. C* **2017**, *121*, 5931–5940. [CrossRef]

34. Pang, W.-L.; Zhang, X.-H.; Guo, J.-Z.; Li, J.-Y.; Yan, X.; Hou, B.-H.; Guan, H.-Y.; Wu, X.-L. *P2*-type $Na_{2/3}Mn_{1-x}Al_xO_2$ cathode material for sodium-ion batteries: Al-doped enhanced electrochemical properties and studies on the electrode kinetics. *J. Power Sources* **2017**, *356*, 80–88. [CrossRef]

35. Kalapsazova, M.; Ortiz, G.F.; Tirado, J.L.; Dolotko, O.; Zhecheva, E.; Nihtianova, D.; Mihaylov, L.; Stoyanova, R. *P3*-Type Layered Sodium-Deficient Nickel-Manganese Oxides: A Flexible Structural Matrix for Reversible Sodium and Lithium Intercalation. *ChemPlusChem* **2015**, *80*, 1642–1656. [CrossRef] [PubMed]

36. Kalapsazova, M.; Ivanova, S.; Kukeva, R.; Simova, S.; Wegner, S.; Zhecheva, E.; Stoyanova, R. Combined use of EPR and Na-23 MAS NMR spectroscopy for assessing the properties of the mixed cobalt-nickel-manganese layers of *P3*-$NayCo_{1-2x}Ni_xMn_xO_2$. *Phys. Chem. Chem. Phys.* **2017**, *19*, 27065–27073. [CrossRef]

37. Kim, E.J.; Ma, L.A.; Duda, L.C.; Pickup, D.M.; Chadwick, A.V.; Younesi, R.; Irvine, J.T.S.; Armstrong, A.R. Oxygen Redox Activity through a Reductive Coupling Mechanism in the *P3*-Type Nickel-Doped Sodium Manganese Oxide. *ACS Appl. Energy Mater.* **2020**, *3*, 184–191. [CrossRef]

38. Lee, D.H.; Xu, J.; Meng, Y.S. An advanced cathode for Na-ion batteries with high rate and excellent structural stability. *Phys. Chem. Chem. Phys.* **2013**, *15*, 3304–3312. [CrossRef]

39. Xu, G.-L.; Amine, R.; Xu, Y.-F.; Liu, J.; Gim, J.; Ma, T.; Ren, Y.; Sun, C.-J.; Liu, Y.; Zhang, X.; et al. Insights into the structural effects of layered cathode materials for high voltage sodium-ion batteries. *Energy Environ. Sci.* **2017**, *10*, 1677–1693. [CrossRef]

40. Huang, Q.; Wang, M.; Zhang, L.; Qi, S.; Feng, Y.; He, P.; Ji, X.; Wang, P.; Zhou, L.; Chen, S.; et al. Shear-resistant interface of layered oxide cathodes for sodium ion batteries. *Energy Storage Mater.* **2022**, *45*, 389–398. [CrossRef]

41. Chen, C.; Ding, Z.; Han, Z.; Liang, C.; Lan, H.; Wang, P.; Gao, P.; Wei, W. Unravelling Atomically Irreversible Cation Migration in Sodium Layered Oxide Cathodes. *J. Phys. Chem. Lett.* **2020**, *11*, 5464–5470. [CrossRef] [PubMed]

42. Hall, T.P.P.; Hayes, W.; Stevenson, R.H.W.; Wilkens, J. Investigation of the Bonding of Iron-Group Ions in Fluoride Crystals. *I. J. Chem. Phys.* **1963**, *38*, 1977. [CrossRef]

43. Zhan, C.; Wu, T.; Lu, J.; Amine, K. Dissolution, migration, and deposition of transition metal ions in Li-ion batteries exemplified by Mn-based cathodes—A critical review. *Energy Environ. Sci.* **2018**, *11*, 243–257. [CrossRef]

44. Jung, R.; Linsenmann, F.; Thomas, R.; Wandt, J.; Solchenbach, S.; Maglia, F.; Stinner, C.; Tromp, M.; Gasteiger, H.A. Nickel, Manganese, and Cobalt Dissolution from Ni-Rich NMC and Their Effects on NMC622-Graphite Cells. *J. Electrochem. Soc.* **2019**, *166*, A378–A389. [CrossRef]

45. Pang, P.; Wang, Z.; Tan, X.; Deng, Y.; Nan, J.; Xing, Z.; Li, H. $LiCoO_2@LiNi_{0.45}Al_{0.05}Mn_{0.5}O_2$ as high-voltage lithium-ion battery cathode materials with improved cycling performance and thermal stability. *Electrochim. Acta* **2019**, *327*, 135018. [CrossRef]